

Geophysical Research Letters



RESEARCH LETTER

10.1029/2020GL090403

Key Points:

- Wavefield gradiometry is applied to arrays of translational seismometers to estimate rotational motions from induced earthquakes
- High-quality records of M0.0 to M1.8 events obtained within 10 km hypocentral distance facilitate array-based resolution of rotation rates
- The obtained apparent phase speed and wave propagation directions are linked to subsurface structure

Supporting Information:

- Supporting Information S1
- Data Set S1

Correspondence to:

G. Hillers,
gregor.hillers@helsinki.fi

Citation:

Taylor, G., Hillers, G., & Vuorinen, T. A. T. (2021). Using array-derived rotational motion to obtain local wave propagation properties from earthquakes induced by the 2018 geothermal stimulation in Finland. *Geophysical Research Letters*, 48, e2020GL090403. <https://doi.org/10.1029/2020GL090403>

Received 26 AUG 2020
 Accepted 10 FEB 2021

Using Array-Derived Rotational Motion to Obtain Local Wave Propagation Properties From Earthquakes Induced by the 2018 Geothermal Stimulation in Finland

G. Taylor^{1,2} , G. Hillers¹ , and T. A. T. Vuorinen¹ 

¹Institute of Seismology, University of Helsinki, Helsinki, Finland, ²Now at Ocean Environment Team, UK Hydrographic Office, Taunton, UK

Abstract We estimate vertical rotation rates for 204 earthquakes that were induced by the 2018 stimulation of the Espoo/Helsinki geothermal reservoir from wavefield gradients across geophone arrays. The array-derived rotation rates from seismograms recorded at 6–9 km hypocentral distances vary between 10^{-9} and 10^{-7} rad s^{-1} , indicating a comparable sensitivity to portable rotational instruments. Using co-located observations of translational and rotational motion, we estimate the local propagation direction and the apparent phase speed of *SH* waves, and compare these estimates with those obtained by *S* wave beamforming. Propagation directions generally align with the earthquake back azimuths, but both techniques show deviations indicative of heterogeneous seismic structure. The rotational method facilitates a station-by-station approach that resolves site specific variations that are controlled by the local geology. We measure apparent *S* wave speeds larger than 5 km s^{-1} , consistent with steep incidence angles and high propagation velocities in the Fennoscandian Shield.

Plain Language Summary Earthquakes generate seismic waves consisting of both translational (back-and-forth) and rotational ground motion. Translational motion is routinely measured by standard seismometers, but the observation of the rotational motion requires relatively expensive and rare instruments. In this study we estimate rotational ground motion caused by earthquakes using groups of translational seismometers. The computation of rotational motion from translational seismometers has been demonstrated before, but the novelty of our study is to use high-quality recordings of earthquakes that were induced by the creation of a geothermal reservoir at 6 km depth in bedrock. We use our measurements of ground rotation to estimate the speed and direction in which the seismic waves are travelling when they reach the seismometers. We find that the direction in which the seismic waves travel usually points back to the earthquake location, but at some seismometers the waves arrive from a different direction. At these locations, it is likely that local geological features are altering the direction of the waves. We expect that our findings will provide access to approaches for determining earthquake characteristics and Earth structure that currently require highly specialized instruments.

1. Introduction

A complete analysis of the seismic wavefield includes observations of translational and rotational motion (Aki & Richards, 2002; Sollberger et al., 2020) for better constraining earthquake source properties (Bernauer et al., 2014; Donner et al., 2016; Huang, 2003; Takeo & Ito, 1997), estimating permanent seismic displacements (Trifunac & Todorovska, 2001), studying ambient seismic noise (Hadziioannou et al., 2012; Tanimoto et al., 2015), and determining Earth's structural properties (Bernauer et al., 2009; Fichtner & Igel, 2009). Many rotational studies utilize data from a ring-laser (Schreiber et al., 2006, 2009) which is typically deployed in geodetic observatories for monitoring Earth's rotation, but these instruments are exceedingly rare, expensive, and are not portable. Though promising portable rotational seismometers are under development (Bernauer et al., 2012, 2018), they are not yet widely available compared to traditional translational sensors.

In the absence of specialized sensors, wavefield gradiometry can be applied to seismic recordings from arrays of three-component translational sensors to provide estimates of rotational motion (Donner et al., 2017; Langston, 2007; Spudich et al., 1995; Suryanto et al., 2006). Modern Large-N deployments of translational sensors promise potential for their use in rotational seismology despite the challenges of the array approach

© 2021. The Authors.

This is an open access article under the terms of the [Creative Commons Attribution-NonCommercial License](https://creativecommons.org/licenses/by-nc/4.0/), which permits use, distribution and reproduction in any medium, provided the original work is properly cited and is not used for commercial purposes.

associated with limited bandwidth and a sensitivity to deployment details. This array-based approach naturally provides co-located translational and rotational measurements, which can be used to estimate source back azimuth and local phase speed through the comparison of transverse acceleration and vertical rotation rates (Hadziioannou et al., 2012; Igel et al., 2005, 2007; Kurrle et al., 2010).

Here, we develop this approach to assess the effectiveness of arrays of translational sensors in a rotational seismology application. Using data from six arrays that were deployed to monitor a geothermal stimulation in the area of Helsinki, Finland (Kwiatek et al., 2019), we aim measure the propagation direction and velocity of horizontally polarized *S* body (*SH*) waves excited by 204 M0.0 to M1.8 induced earthquakes, at hypocentral distances of 6–9 km. We compare the results of the rotational approach to those of classic beamforming applied to the same *S* wave data, and compare the back azimuth estimates against the great-circle direction of each event. Where previous studies have focused on comparatively small numbers of large events recorded at regional or teleseismic distances, or focused on Love wave observations recorded on rotational instruments, our study innovates to include the application of array-derived rotation (ADR) measurements to a large earthquake data set collected at small distances, as well as utilizing body wave observations. We believe this study demonstrates the effectiveness of ADR methods in the highly relevant application of characterizing induced seismicity.

2. Array-Derived Rotation (ADR): Theory and Methods

Transversely polarized plane waves propagating in homogeneous media with amplitude A , wavenumber k , and phase speed c exhibit a proportional relationship between the transverse component of ground acceleration, a_t , and the rotation rate about the vertical axis, $\dot{\omega}_z$ (Igel et al., 2005; Sollberger et al., 2018),

$$\frac{a_t}{\dot{\omega}_z} = \frac{-k^2 c^2 A \sin(kx - kct)}{\frac{1}{2} k^2 c A \sin(kx - kct)} = -2c. \quad (1)$$

Hence, when the transverse recording component is correctly aligned to be perpendicular to the propagation direction, a_t and $\dot{\omega}_z$ will have the same waveform and differ only in amplitude by the factor $-2c$. Equation 1 suggests that it is possible to use point recordings of horizontally polarized waves to estimate the source direction θ and the apparent local phase speed, c_a , by maximizing the similarity between co-located recordings of a_t and $\dot{\omega}_z$ (Hadziioannou et al., 2012; Igel et al., 2007; Kurrle et al., 2010).

Rotational motion ω_z at the free surface can be estimated using the gradients in the horizontal displacement wavefield recorded by an array of seismometers deployed in an arbitrary geometry (Cochard et al., 2006; Spudich et al., 1995)

$$\omega_z = \frac{1}{2} \left(\frac{\partial u_y}{\partial x} - \frac{\partial u_x}{\partial y} \right). \quad (2)$$

The partial derivatives can be computed by solving the inverse problem (Langston & Liang, 2008; Liang & Langston, 2009)

$$\begin{pmatrix} u_1 - u_0 \\ u_2 - u_0 \\ \vdots \\ u_N - u_0 \end{pmatrix} = \begin{pmatrix} \delta x_1 & \delta y_1 \\ \delta x_2 & \delta y_2 \\ \vdots & \vdots \\ \delta x_N & \delta y_N \end{pmatrix} \begin{pmatrix} \partial u / \partial x \\ \partial u / \partial y \end{pmatrix}, \quad (3)$$

where u_0 is the displacement at the reference location x_0, y_0 and $u_i, i = 1, \dots, N$ is the displacement at the i th receiver in the $N + 1$ station array. δx_i and δy_i are the difference in the x - and y -coordinates between the reference station and station i . Equation 3 is of the form $d = Gm$ and can be solved by common least squares inversion methods. The ADR approach requires sufficiently large wavelength-to-aperture ratios to ensure smoothly varying gradients to properly describe the array deformation by spatially uniform rigid body rotation (Donner et al., 2017; Langston, 2007; Spudich & Fletcher, 2008), and the data acquisition should support the resolution of the systematic horizontal amplitude differences (Langston, 2018).

We combine these principles for estimating propagation direction θ and velocity c_a at an array of seismometers considering any one sensor as reference station:

1. Using Equation 3, calculate $\partial_x u_y$ and $\partial_y u_x$, where u_y and u_x are the North and East component of motion
2. Use Equation 2 to compute ω_z from these $\partial_x u_y$ and $\partial_y u_x$ estimates, which is differentiated to obtain the vertical rotation rate, $\dot{\omega}_z$
3. Grid search over source back azimuths between 0° and 360° . For each back azimuth, calculate a_t , the transverse component of acceleration, and cross-correlate the a_t and $\dot{\omega}_z$ waveforms. The back azimuth that corresponds to the largest cross-correlation coefficient is an estimate of the local propagation direction θ
4. Calculate c_a for the best-fitting back azimuth solving Equation 1 in a least squares sense from a 1 s window centered on the maximum S wave amplitude through

$$c_a = \frac{\sum_t a_t(t) \dot{\omega}_z(t)}{2 \sum_t \dot{\omega}_z(t)^2}. \quad (4)$$

Alternative ADR implementations have been suggested for improved robustness and error assessment. This includes a regression scheme for the simultaneous estimate of θ and c_a (Wassermann et al., 2016); inversions yielding array averages that are possibly less sensitive to outliers compared to our arithmetic average over the $N + 1$ estimates (Spudich et al., 1995), and that take the non-homogeneous nature of strain and rotation from a propagating wave into account (Langston, 2018); and schemes that account and correct for strain-rotation coupling (Schmelzbach et al., 2018; Singh et al., 2020; Sollberger et al., 2015). Here, however, the overall high data quality underpins our successful application of the above ADR implementation for local θ and c_a estimates at six array sites, suggesting that this type of analysis can complement other array-based processing techniques used to study local wave propagation (Capon, 1969; Langston & Liang, 2008; Riahi et al., 2013; Wagner, 1998).

3. Data from the 2018 Espoo/Helsinki Geothermal Reservoir Stimulation

Between June 4 and July 22, 2018, the St1 Deep Heat Oy company stimulated a 6.1 km deep geothermal reservoir in the Espoo/Helsinki region of southern Finland (Kwiatek et al., 2019). The Institute of Seismology at the University of Helsinki (ISUH) deployed a temporary network of ~ 100 4.5 Hz three-component geophones—‘Cube’ stations from the Geophysical Instrument Pool Potsdam (GIPP)—between May 7 and August 20, 2018 (Hillers et al., 2020). For this study, we use data from six arrays (Figure 1), three large arrays nominally consisting of 25 stations (SS, EV, and TL) and three arrays of four stations (PM, PK, and RS), that were installed on crystalline bedrock outcrops characteristic of the Fennoscandian Shield (Hillers et al., 2020; Tiira et al., 2020). The array aperture is ~ 100 m, and the interstation distance ~ 25 m. The geophone orientations follow magnetic compass readings and meet the standards for portable broadband seismometer installations (Wielandt, 2012). All stations operate at the same 400 Hz sampling rate and with a uniform gain. A total of ~ 2900 induced seismic events were automatically detected by ISUH routine analysis. A subset of the 204 largest events was selected for magnitude and location estimation (Hillers et al., 2020; Supporting Information S1). We apply the method outlined in Section 2 to these events, which have a local magnitude range between $M_{0.0}$ and $M_{1.8}$ and source-receiver distances of 6–9 km.

The absence of a sedimentary layer throughout the region results in high-quality seismograms (Figure 2a). The 5%, median, and 95% signal-to-noise ratios (SNR) in dB of vector-combined 2–15 Hz horizontal velocity seismograms at the large arrays EV ($\sim 4,270$ combined seismograms at all stations), SS (4,000), and TL (4,090) are, respectively, 13/26/45, 18/31/48, and 17/38/53. For the three small arrays PM (780), PK (760), and RS (750) the ratios are 15/26/43, 15/29/48, and 18/32/51, respectively. Signal power is the average squared amplitude of these seismograms in a 1 s long S wave window. The noise level is similarly estimated as the 25-percentile of the distribution obtained with a 10 s long moving window across a 5 min long window starting 1 min before the P wave arrival.

Prior to applying ADR, we correct the raw ground velocity records for the instrument response, perform frequency domain integration and differentiation to obtain displacement and acceleration, and apply a zero-phase butterworth bandpass filter between 2 and 15 Hz (Figure 2a). The 2 Hz low-frequency limit

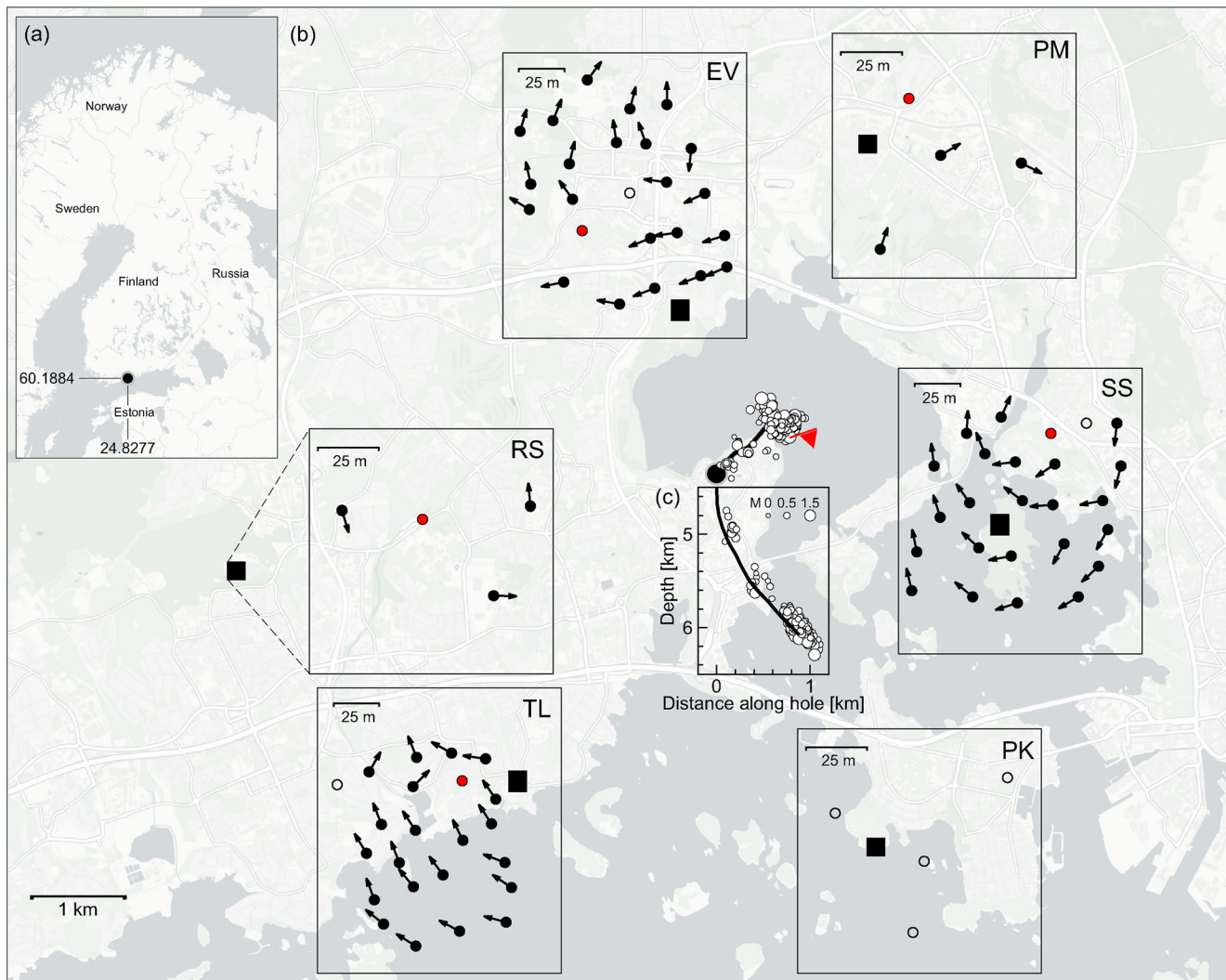


Figure 1. (a) Location of the study area in southern Finland. The coordinates indicate the wellhead. (b) Map of the study area. The central black circle marks the wellhead, the attached line shows the borehole trajectory between 4.8 and 6.1 km depth, and the white circles are epicenters of the analyzed earthquakes. The red flag marks the largest event. Solid black rectangles indicate array locations (not to scale). The corresponding station distributions are shown in the insets, and the arrows visualize the displacement variations observed for the largest event. The red circles show the reference station, and the open circles indicate missing data for this event. EV, PM, SS, PK, TL, and RS abbreviate the locations Elfvik, Pajamäki, Seurasaari, Poliisin kesäkoti, Toppelund, and Rudolf-Steiner school Espoo, respectively. (c) Depth cross-section of the borehole trajectory and seismicity.

is related to the instrument performance (Poppeliers & Evans, 2015; Ringler et al., 2016). At 15 Hz the wavelength-to-aperture ratio measured along the surface for the six arrays is between 3.2 and 7.7 assuming straight rays and a S wave velocity of 3.3 km s^{-1} (Hillers et al., 2020), which ensures sufficiently smooth gradients (Donner et al., 2017; Spudich & Fletcher, 2008). We work with 3 s long seismograms starting 0.5 s before the manually picked P wave arrival. Our maximum observed horizontal displacements generally vary between 10^{-8} and 10^{-6} m. From these the vertical rotation is calculated by applying Equation 3 then Equation 2, using all N records for each reference station. We perform the back azimuth grid search with an increment of 1° (Figure 2). The obtained estimates are not sensitive to the choice of window length, as long as the full S waveform is included.

We compare the directions and velocities estimated by ADR analysis with those calculated from conventional beamforming, as well as the great-circle direction indicated by the earthquake locations of Hillers et al. (2020). For the beamforming results, we process the North and East component waveforms exactly as for the rotational analysis, and apply time-domain delay-and-sum beamforming to a 0.5 s long window

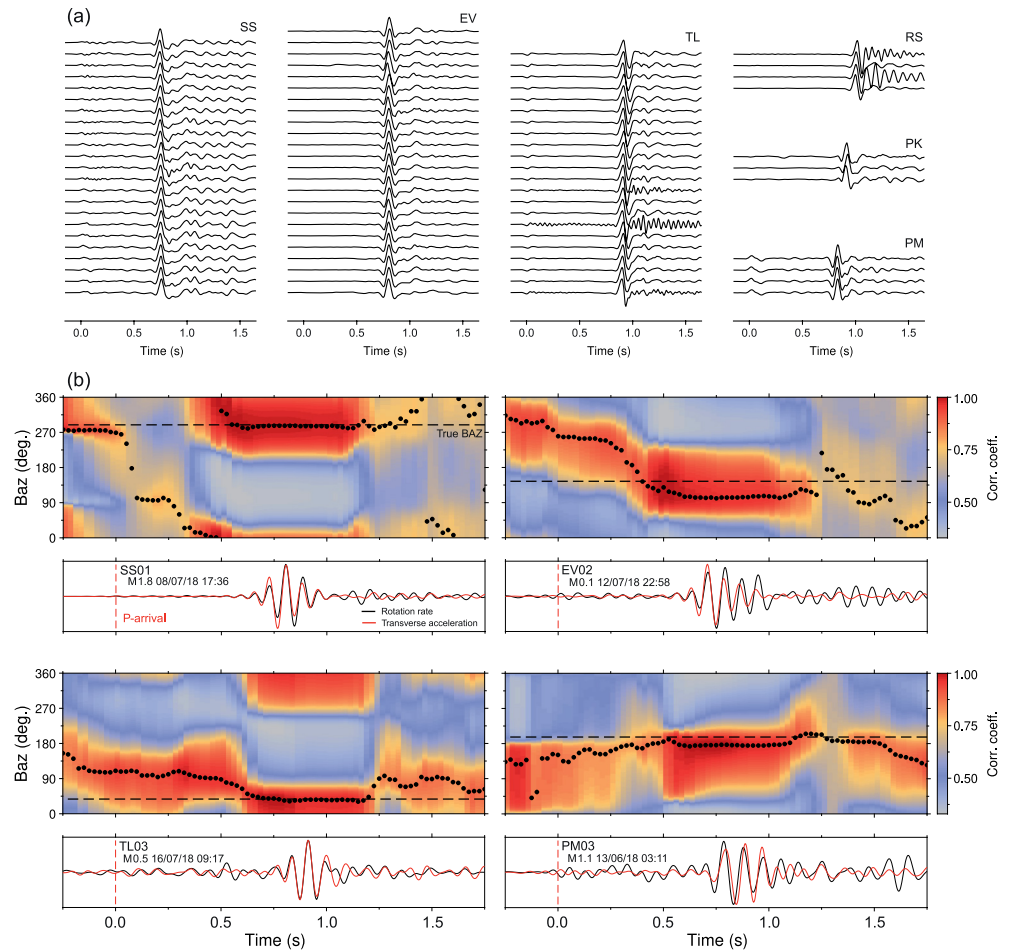


Figure 2. (a) *P* wave aligned N-component displacement seismograms of the largest M1.8 event show clean, high-SNR *S* waveforms in the target frequency band. (b) Array-derived vertical rotation rate ($\dot{\omega}_z$, black line) for four station-event pairs, compared to the best-fitting transverse acceleration seismogram (a_t , red line). Amplitudes are normalized for comparison. The colors show the correlation coefficient between $\dot{\omega}_z$ and a_t as a function of time and event back azimuth (Baz), estimated in overlapping 0.5 s windows. The black dots indicate the back azimuth with the highest correlation coefficient in each window. The great-circle direction is indicated with the dashed black line. SNR, signal-to-noise ratio.

centered on the manually picked *S* wave arrival. Our tests show that results from different choices of wave type, component, or frequency band can vary due to the sensitivity to different propagation effects. However, our observations generally agree with the vertical component *P* wave beamforming results obtained by Hillers et al. (2020) using data from 6 $M \geq 1.1$ events, which supports our comparison of the ADR and beamforming methods applied to the same *S* waveforms.

The ADR method produces direction and velocity estimates for every reference station in an array, whereas beamforming provides one estimate per array. We present both array-average (Figure 3) and station-by-station (Figure 4) estimates for the rotational approach to assess if the array-average results show improved accuracy, and to test if systematic variations in propagation direction across an array can be resolved. The station-by-station results do not systematically depend on the relative position of the reference station in each array which supports the choice of the high-frequency limit.

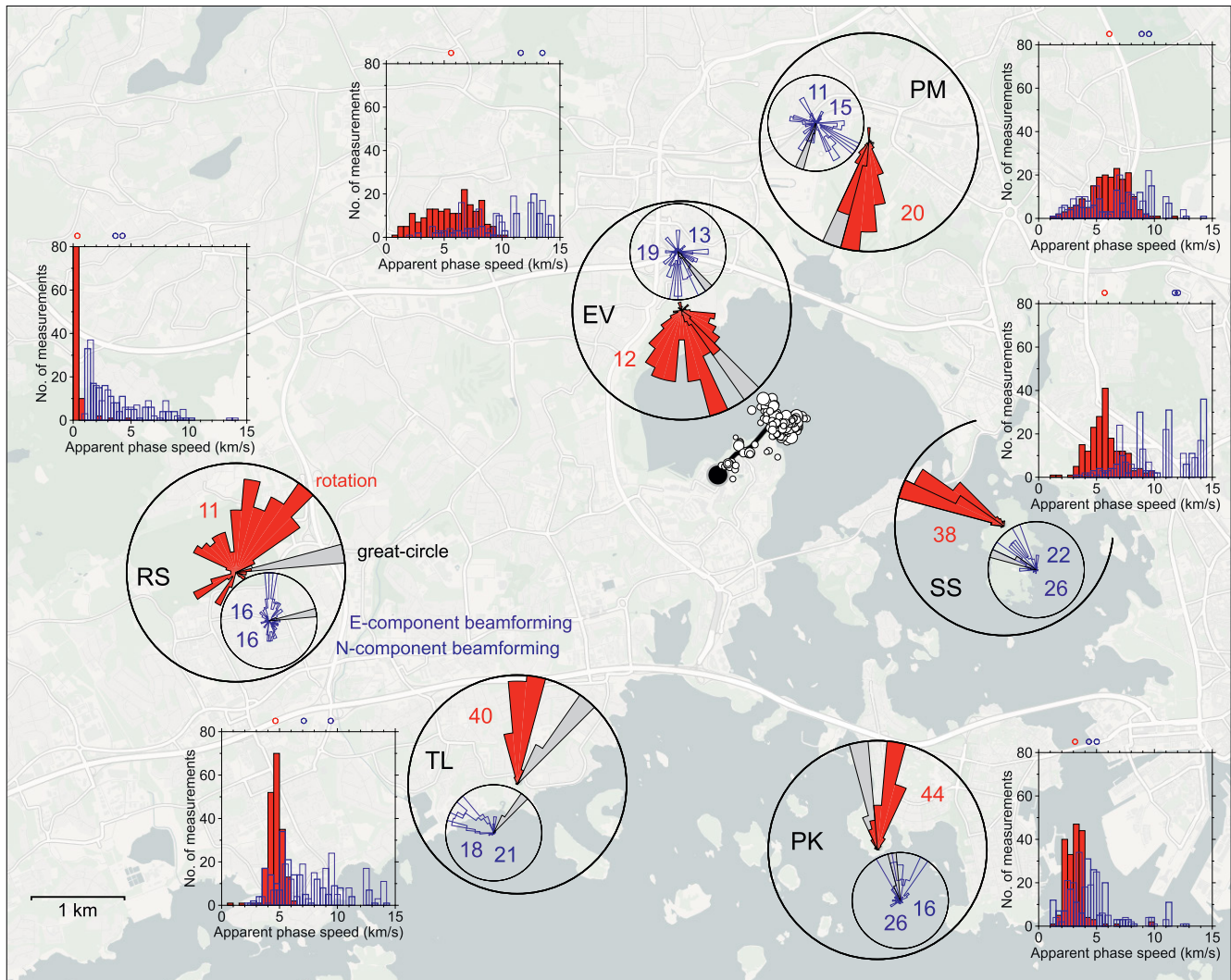


Figure 3. The large rose-diagrams show back azimuth distributions obtained with array-average rotational motion (red). These diagrams are centered on the array locations. The small, offset rose-diagrams show the back azimuth distributions obtained with *S* wave beamforming (blue). Both diagrams show distributions of the great-circle back azimuth between the array center and the earthquakes (gray). All diagrams are scaled to the maximum value in each distribution. The bin-width is 10°. The numbers are the ratio of the peak bin value to the total sum in percent. The histograms show the distributions of the obtained apparent phase velocity using the same color code. The small circles on top of the frames indicate averages.

4. Results

4.1. Array-Derived Rotational Motion for the Induced Earthquakes

To illustrate the process, we first present some of the intermediate results for the largest M1.8 event. Figure 1 shows the direction of the maximum displacement variation of the *S* wave arrival from the red-indicated reference receiver at x_0, y_0 in each array. These observed displacement variations are the left-hand side of Equation 3 used to calculate the gradients and then the vertical rotation rate (Equation 2). The differential displacements shown in Figure 1 exhibit a mix of linear and rotational components of motion. We tend to interpret the circular pattern at the SS array not as manifestation of a uniform rigid body rotation around the reference location. This pattern rather indicates the violation of the assumed plane *SH* wave motion that possibly interferes with *SV* motion (Hillers et al., 2020).

However, Figures 2b and 3 demonstrate that the approach produces consistent, robust estimates of the *S* wave propagation direction. Figure 2b shows array-derived $\dot{\omega}_z$ estimates (black waveforms) at several locations, calculated from Equation 3, for four events between M0.1 and M1.8. The figure also shows the

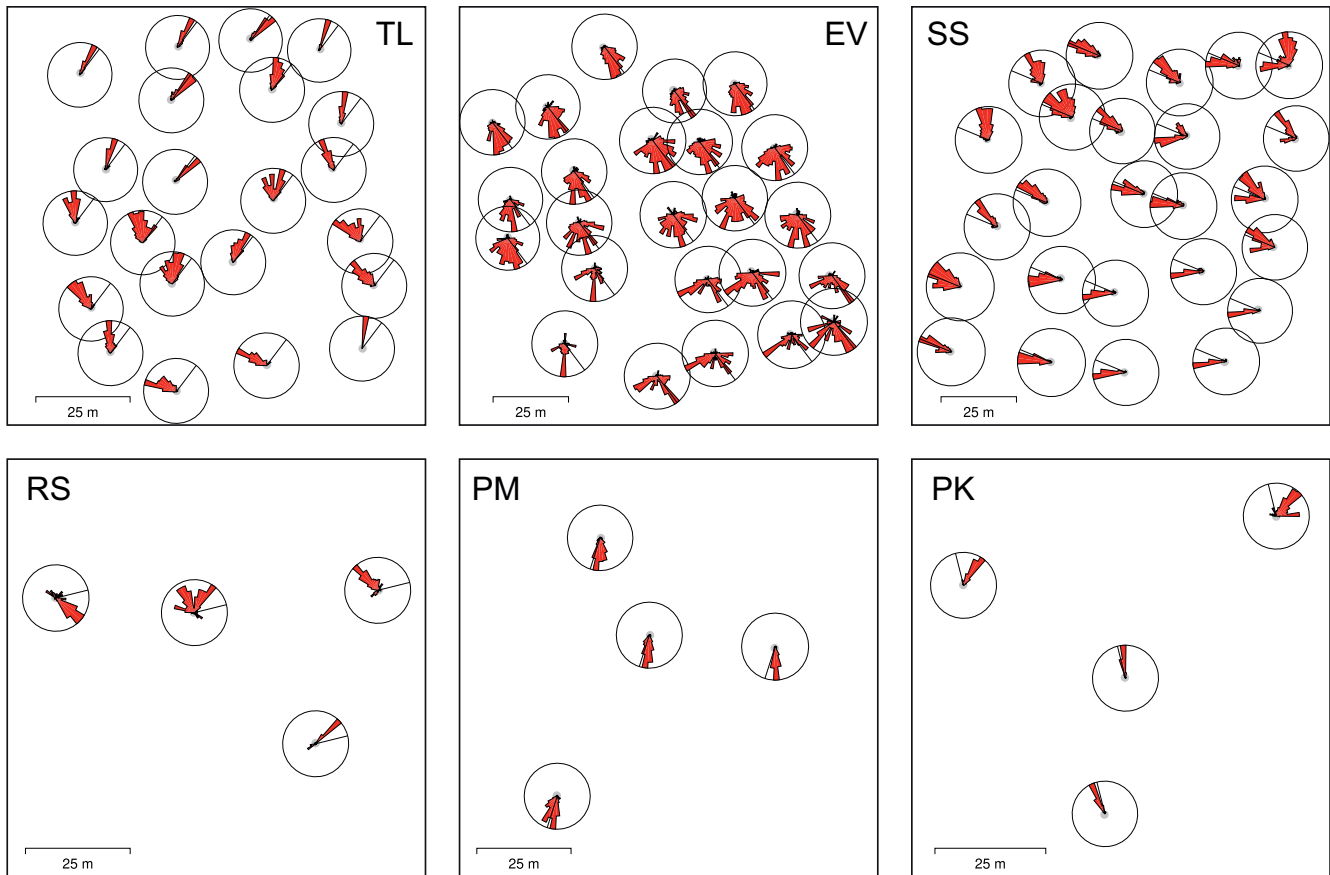


Figure 4. The rose diagrams show the station-by-station misfit between the observed propagation direction estimated by the rotational method and the great-circle event back azimuth. The black line in the rose diagram indicates the mean event back azimuth of all 204 events at that station. A misfit of 0° aligns with that black line. Large and small arrays are ordered from west to east.

transverse acceleration a_t (red waveforms) that best matches the calculated $\dot{\omega}_z$. The shape of the S waveforms of $\dot{\omega}_z$ and a_t are nearly identical, similar to the broadband seismometer and ring-laser observations of Igel et al. (2007). The maximum S wave vertical rotation rate amplitude at station SS01 for the M1.8 event is $\sim 6 \times 10^{-7}$ rad s^{-1} . Generally, our estimated maximum rotation rates lie in a range of 10^{-9} to 10^{-7} rad s^{-1} for the events between magnitude M0.0 and M1.8, respectively. Also shown in Figure 2b is the time dependent local propagation direction θ that is estimated by maximizing the similarity between $\dot{\omega}_z$ and a_t in overlapping 0.5 s windows. The consistency of the dotted and dashed lines in Figure 2b shows that for these events and stations, θ aligns closely with the earthquake back azimuth during the passage of the S wave train, with a maximum deviation of $\sim 30^\circ$ for the EV02 example in Figure 2b. The azimuth patterns regularly exhibit a stable estimate preceding the main S wave arrival which is attributable to P - S scattered energy (Igel et al., 2005; Igel et al., 2007; Pham et al., 2009).

4.2. Application to the Full Data Set

Figure 3 compiles the array-averaged back azimuths estimated by the rotational method, beamforming, and the great-circle directions for all 204 events. The root-mean-square misfit of the rotational estimates compared to the great-circle azimuth varies between 16.6° for the SS array, to 93.2° for the RS array. Similar to the P wave beamforming results in Hillers et al. (2020), the majority of the ADR and beamforming results at the EV, PM, SS, and EV arrays are broadly consistent with the great-circle direction. The deviations at the TL and RS arrays can be controlled by path effects, local medium heterogeneity, or coupling problems, and are revisited below. The rotational approach generally outperforms beamforming, with an average improvement in misfit of 39% and 36% for the North and East component beamforming. Better ADR performance

can also be inferred from the contrast between the overall more narrow range of ADR results compared to the greater range of values of beamforming back azimuths. This contrast is largest at the EV and PM arrays in close vicinity to the source volume, which suggests the ADR performance is more stable at near-vertical incidence, where the beamformer output has a higher sensitivity to processing parameters such as window length or the discretization of the slowness domain.

The ADR velocity estimates (red histograms in Figure 3) between 4 and 6 km s⁻¹ are higher than the *S* wave velocity of 3 km s⁻¹ (Hillers et al., 2020; Kwiatek et al., 2019), but are consistent with the steep incidence. The angles of incidence also explain that arrays SS, EV, and PM all record mean apparent phase speeds close to 6 km s⁻¹, whilst TL and PK record lower phase speeds between 3 and 5 km s⁻¹ at greater hypocentral distances. At array RS, the rotational approach produces spurious apparent phase speeds below 0.1 km s⁻¹, indicating that factors such as the known poorer instrument coupling are affecting the waveforms and the overall inconsistent estimates at this location (Figures 2a and 4).

The blue beamforming histograms in Figure 3 show generally much broader distributions which again suggests the ADR method is able to produce more stable—narrowly distributed—array-average estimates; the comparatively wide ADR distribution at the EV array is attributed to the complex geology of the site (Elminen et al., 2008), which can also explain the variations in local propagation directions discussed in the next paragraph.

Figure 4 shows clear patterns in the residual difference between the rotational back azimuth estimates and the great-circle path across each array. At the TL array, a strong north-south variation in the residual is evident. In the northern part the estimates align well with the great-circle direction (black line in the rose diagram), whereas the southern stations show a systematic offset of up to -100°. We conclude that local inhomogeneities influence the array-averaged ADR directions and also the beamforming directions in Figure 3. The EV array shows another north-south pattern that correlates well with quality estimates for the data recorded at this site (Figure 4c in Hillers et al., 2020). We attribute this pattern to the local geology. The northern stations are installed on bedrock, whilst the southern stations are situated on a west-east aligned shear system (Elminen et al., 2008) which we think is responsible for the west-east dominance in differential motion (Figure 1) and local wave propagation direction (Figure 4). In contrast to the strong variations at these two sites, the SS array pattern appears more homogeneous. Still, some stations located in the northern half show systematic deviations of up to +45° from the reference average great-circle direction, whereas stations in the south-eastern quadrant show a consistent residual pattern with deviations of -30°. For the small arrays, the inconsistent RS results again point to installation deficits, the PM observations impress by their homogeneity and consistency, and the estimates at PK imply systematic local effects.

5. Discussion

Our results demonstrate that by applying wavefield gradiometry to arrays of geophones, it is possible to measure vertical rotation rates as low as 10⁻⁹ rad s⁻¹, which approaches the sensitivity of portable rotational sensors (Bernauer et al., 2018). Such sensitivity demonstrates that inexpensive translational sensors can be an effective substitute for rotational instruments in weak-motion seismology until reliable commercial rotational sensors become more widely available. In theory, three stations is the minimum requirement for estimating rotational motion, and we have established that it is possible to obtain a rotational sensitivity of 10⁻⁹ rad s⁻¹ using the small four-station arrays. Compared to the 53.8° average RMS back azimuth misfit from the great-circle direction at the three small arrays, however, the average 35.6° at the large arrays implies that a larger station count tends to provide a more accurate estimate of vertical rotation rate. Our array-averaged results of back azimuth and phase speed exhibit a smaller variance compared to observations on a station-by-station basis, which has also been noted in studies that directly compare array-derived rotation estimates with co-located ring-laser observations (Donner et al., 2017; Suryanto et al., 2006).

The most restrictive constraint on ADR measurements are the limitations on the frequency content of the signal. The computation of wavefield gradients requires smooth variation in the displacement wavefield over the array (Liang & Langston, 2009), which is achieved by limiting the analysis to wavelengths larger than the array size. This makes the aperture the primary control on the high frequency content, whereas the low frequency limit on accurate ADR estimates is related to the instrument characteristics (Poppeliers

& Evans, 2015; Ringler et al., 2016). These restrictions on the use of ADR measurements in applications such as Love wave dispersion estimation, where broadband rotational instruments remain at an advantage (Wassermann et al., 2016), can partially be accommodated by hierarchical array geometries and the use of sub-arrays to increase the spectral bandwidth. Further challenges to the ADR approach concern the effects of sensor misorientations (Langston, 2018), correlated noise, and wavefront planarity.

Here, the signatures of structural variations obtained with the ADR station-by-station approach, for example, at the EV array, imply that the assumption of plane wave propagation through a homogeneous subsurface that underpins both the beamforming algorithm and the ADR finite-difference approximation is likely inaccurate. ADR yields on average more consistent estimates of the source back azimuth compared to our conventional *S* wave beamforming implementation, although using a different wave type, component of motion, or frequency band can improve the beamforming results. Our beamforming tests using vertical component *S* wave data (not shown) suggest that further comparisons of ADR and beamforming results, supported by synthetics, are needed to study the sensitivities of the different waveforms and methods. The data quality and network configuration allow complementary, systematic performance tests of a diverse range of array techniques to study wave propagation and wave attributes (Langston & Liang, 2008; Riahi et al., 2013; Wagner, 1998).

Localized near-receiver heterogeneity is known to bias rotational motions resolved by individual rotational and translational sensors through strain-rotation coupling (van Driel et al., 2012). Mitigation schemes help provide more accurate measurements (Schmelzbach et al., 2018; Singh et al., 2020; Sollberger et al., 2015), where the ADR approach has the additional option to average out such effects. Systematic variations between the estimated and great-circle directions can be used to infer large scale variations in seismic velocity between the source and receiver array (Boué et al., 2014; Liang & Langston, 2009). Separating between such systematic variations, and those which affect individual stations or groups of stations differently, facilitates the distinction between the variations outside of the array and site specific aberrations; observations at the EV and TL arrays provide illustrative examples. We anticipate that the accessibility of local wave propagation characteristics will further incentivize the analysis of densely sampled rotational motion in determining small-scale structural variations, for example, in fault zones (Roux et al., 2016) or mining environments (Singh et al., 2019).

6. Conclusions

Using high-quality records of 204 small-magnitude induced earthquakes we have demonstrated that arrays of translational seismic sensors can be used to estimate rotational motion with sufficient accuracy for practical weak-motion seismic applications. Our observations of vertical rotational motion at 2–15 Hz excited by earthquakes as small as $M_{0.0}$ at hypocentral distances of 6–9 km include measurements of vertical rotation rates down to 10^{-9} rad s^{-1} , indicating that the sensitivity of array-derived rotation measurements is comparable to portable rotational sensors. Our earthquake back azimuth estimates from the array-derived rotation approach are consistently more accurate than those obtained from conventional *S* wave beamforming, with an average improvement in misfit of $\sim 40\%$, and the rotation-based station-by-station observations help to study local wave propagation phenomena. Our data suggest the extension of the array analysis to resolve rotational motion around all three axes (Spudich et al., 1995). Robust array observations of six-component motion can then lead to better inversions of moment tensors (Cochard et al., 2006; Donner et al., 2016; Ichinose et al., 2020) and thus improved source mechanism estimates of the induced earthquakes.

Acknowledgments

The 100 short-period sensors and the DATA-CUBE3 loggers were provided by the Geophysical Instrument Pool Potsdam (GIPP) under the Grant 201802. This research was supported by the Academy of Finland (decision no. 337913). We thank S. Donner, C. Hadziioannou, and F. Bernauer for insightful discussions, and C. Langston, an anonymous reviewer, and H. Igel for comments that helped improve the manuscript.

Data Availability Statement

The full data set can be accessed after the GIPP moratorium period from the GIPP repository following Hillers et al. (2019). A supplementary file to this publication provides the origin times and locations of the events used in this study. Parts of the analysis were implemented using ObsPy (Krischer et al., 2015).

References

Aki, K., & Richards, P. G. (2002). *Quantitative Seismology* (2nd ed.). Sausalito, CA: University Science Books.

- Bernauer, F., Wassermann, J., Guattari, F., Frenois, A., Bigueur, A., Gaillot, A., et al. (2018). BlueSeis3A: Full characterization of a 3C broadband rotational seismometer. *Seismological Research Letters*, 89, 620–629. <https://doi.org/10.1785/0220170143>
- Bernauer, M., Fichtner, A., & Igel, H. (2009). Inferring earth structure from combined measurements of rotational and translational ground motions. *Geophysics*, 74, WCD41–WCD47. <https://doi.org/10.1190/1.3211110>
- Bernauer, M., Fichtner, A., & Igel, H. (2014). Reducing nonuniqueness in finite source inversion using rotational ground motions. *Journal of Geophysical Research: Solid Earth*, 119, 4860–4875. <https://doi.org/10.1002/2014JB011042>
- Bernauer, M., Wassermann, J., & Igel, H. (2012). Rotational sensors: A comparison of different sensor types. *Journal of Seismology*, 16, 595–602. <https://doi.org/10.1007/s10950-012-9286-7>
- Boué, P., Roux, P., Campillo, M., & Briand, X. (2014). Phase velocity tomography of surface waves using ambient noise cross correlation and array processing. *Journal of Geophysical Research: Solid Earth*, 119, 519–529. <https://doi.org/10.1002/2013JB010446>
- Capon, J. (1969). High-resolution frequency-wavenumber spectrum analysis. *Proceedings of the IEEE*, 57(8), 1408–1418. <https://doi.org/10.1109/PROC.1969.7278>
- Cochard, A., Igel, H., Schuberth, B., Suryanto, W., Velikoseltsev, A., Schreiber, U., et al. (2006). Rotational motions in seismology: Theory, observation, simulation. In R. Teisseyre, E. Majewski, & M. Takeo, Eds., *Earthquake source asymmetry, structural media and rotation effects* (pp. 391–411). Berlin/Heidelberg: Springer. https://doi.org/10.1007/3-540-31337-0_30
- Donner, S., Bernauer, M., & Igel, H. (2016). Inversion for seismic moment tensors combining translational and rotational ground motions. *Geophysical Journal International*, 207, 562–570. <https://doi.org/10.1093/gji/ggw298>
- Donner, S., Lin, C.-J., Hadziioannou, C., Gebauer, A., Vernon, F., Agnew, D. C., et al. (2017). Comparing direct observation of strain, rotation, and displacement with array estimates at Piñon Flat Observatory, California. *Seismological Research Letters*, 88, 1107–1116. <https://doi.org/10.1785/0220160216>
- Elminen, T., Airo, M.-L., Niemelä, R., Pajunen, M., Vaarma, M., Wasenius, P., & Wennerström, M. (2008). Fault structures in the Helsinki area, southern Finland. *Geological Survey Finland Special Paper*, 47, 185–213.
- Fichtner, A., & Igel, H. (2009). Sensitivity densities for rotational ground-motion measurements. *Bulletin of the Seismological Society of America*, 99, 1302–1314. <https://doi.org/10.1785/0120080064>
- Hadziioannou, C., Gaebler, P., Schreiber, U., Wasserman, J., & Igel, H. (2012). Examining ambient noise using colocated measurements of rotational and translational motion. *Journal of Seismology*, 16, 787–796. <https://doi.org/10.1007/s10950-012-9288-5>
- Hillers, G., Vuorinen, T. A. T., Arola, E. J., Katajisto, V. E., Koskenniemi, M. P., McKeivitt, B. M., et al. (2019). A 100 3-component sensor deployment to monitor the 2018 EGS stimulation in Espoo/Helsinki, southern Finland. <https://doi.org/10.5880/GIPP.201802.1>
- Hillers, G., Vuorinen, T. A. T., Uski, M. R., Kortström, J. T., Mäntyniemi, P., Tiira, T., et al. (2020). The 2018 geothermal reservoir stimulation in Espoo/Helsinki, southern Finland: Seismic network anatomy and data features. *Seismological Research Letters*, 91, 770–786. <https://doi.org/10.1785/0220190253>
- Huang, B.-S. (2003). Ground rotational motions of the 1999 Chi-Chi, Taiwan earthquake as inferred from dense array observations. *Geophysical Research Letters*, 30. <https://doi.org/10.1029/2002GL015157>
- Ichinose, G. A., Ford, S. R., & Mellors, R. J. (2020). Regional moment tensor inversion using rotational observations. *Journal of Geophysical Research: Solid Earth*, 126(2), e2020JB020827. <https://doi.org/10.1029/2020JB020827>
- Igel, H., Cochard, A., Wasserman, J., Flaws, A., Schreiber, U., Velikoseltsev, A., & Dinh, N. P. (2007). Broad-band observations of earthquake-induced rotational ground motions. *Geophysical Journal International*, 168, 182–196. <https://doi.org/10.1111/j.1365-246X.2006.03146.x>
- Igel, H., Schreiber, U., Flaws, A., Schuberth, B., Velikoseltsev, A., & Cochard, A. (2005). Rotational motions induced by the M8.1 Tokachi-oki earthquake, September 25, 2003. *Journal of Geophysical Research*, 32. <https://doi.org/10.1029/2004GL022336>
- Krischer, L., Megies, T., Barsch, R., Beyreuther, M., Lecocq, T., Caudron, C., & Wassermann, J. (2015). ObsPy: A bridge for seismology into the scientific Python ecosystem. *Computational Science & Discovery*, 8(1). <https://doi.org/10.1088/1749-4699/8/1/014003>
- Kurrle, D., Igel, H., Ferreira, A. M. G., Wasserman, J., & Schreiber, U. (2010). Can we estimate local Love wave dispersion properties from colocated amplitude measurements of translations and rotations? *Geophysical Research Letters*, 37. <https://doi.org/10.1029/2009GL042215>
- Kwiatak, G., Saarno, T., Ader, T., Bluemle, F., Bohnhoff, M., Chendorain, M., et al. (2019). Controlling fluid-induced seismicity during a 6.1-km-deep geothermal stimulation in Finland. *Science Advances*, 5(5), eaav7224. <https://doi.org/10.1126/sciadv.aav7224>
- Langston, C. A. (2007). Wave gradiometry in two dimensions. *Bulletin of the Seismological Society of America*, 97, 401–416. <https://doi.org/10.1785/0120060138>
- Langston, C. A. (2018). Calibrating dense spatial arrays for amplitude statics and orientation errors. *Journal of Geophysical Research: Solid Earth*, 123, 3849–3870. <https://doi.org/10.1002/2017JB015098>
- Langston, C. A., & Liang, C. (2008). Gradiometry for polarized seismic waves. *Journal of Geophysical Research*, 113. <https://doi.org/10.1029/2007JB005486>
- Liang, C., & Langston, C. A. (2009). Wave gradiometry for USArray: Rayleigh waves. *Journal of Geophysical Research*, 114. <https://doi.org/10.1029/2008JB005918>
- Pham, N., Igel, H., Wassermann, J., Käser, M., de la Puente, J., & Schreiber, U. (2009). Observations and modeling of rotational signals in the P coda: constraints on crustal scattering. *Bulletin of the Seismological Society of America*, 99, 1315–1332. <https://doi.org/10.1785/0120080101>
- Poppeliers, C., & Evans, E. V. (2015). The effects of measurement uncertainties in seismic wave gradiometry. *Seismological Research Letters*, 105, 3143–3155. <https://doi.org/10.1785/0120150043>
- Riahi, N., Bokelmann, G., Sala, P., & Saenger, E. H. (2013). Time-lapse analysis of ambient surface wave anisotropy: A three-component array study above an underground gas storage. *Journal of Geophysical Research: Solid Earth*, 118, 5339–5351. <https://doi.org/10.1002/jgrb.50375>
- Ringler, A., Wildon, D., Storm, T., Marshall, B. T., Hutt, C. R., & Holland, A. (2016). Noise reduction in long-period seismograms by way of array summing. *Bulletin of the Seismological Society of America*, 106. <https://doi.org/10.1785/0120160129>
- Roux, P., Moreau, L., Lecointre, A., Hillers, G., Campillo, M., Ben-Zion, Y., et al. (2016). A methodological approach toward high-resolution seismic imaging of the San Jacinto Fault Zone using ambient-noise recordings at a spatially dense array. *Geophysical Journal International*, 206, 980–992. <https://doi.org/10.1093/gji/ggw193>
- Schmelzbach, C., Donner, S., Igel, H., Sollberger, D., Taufiqurrahman, T., Bernauer, F., et al. (2018). Advances in 6C seismology: Applications of combined translational and rotational motion measurements in global and exploration seismology. *Geophysics*, 83, WC53–WC69. <https://doi.org/10.1190/GEO2017-0492.1>
- Schreiber, K. U., Hautmann, J. N., Velikoseltsev, A., Wassermann, J., Igel, H., Otero, J., et al. (2009). Ring laser measurements of ground rotations for seismology. *Bulletin of the Seismological Society of America*, 99, 1190–1198. <https://doi.org/10.1785/0120080171>

- Schreiber, K. U., Stedman, G. E., Igel, H., & Flaws, A. (2006). Ring laser gyroscopes as rotation sensors for seismic wave studies. In R. Teisseyre, E. Majewski, & M. Takeo, Eds., *Earthquake source asymmetry, structural media and rotation effects* (pp. 377–390). Berlin/Heidelberg: Springer Verlag.
- Singh, B., Malinowski, M., Hloušek, F., Koivisto, E., Heinonen, S., Hellweg, O., et al. (2019). Sparse 3D seismic imaging in the Kylahti mine area, Eastern Finland: Comparison of time versus depth approach. *Minerals*, 9(305). <https://doi.org/10.3390/min9050305>
- Singh, S., Capdeville, Y., & Igel, H. (2020). Correcting wavefield gradients for the effects of local small-scale heterogeneities. *Geophysical Journal International*, 220, 996–1011. <https://doi.org/10.1093/gji/ggz479>
- Sollberger, D., Greenhalgh, S., Schmelzbach, C., Renterghem, C. V., & Robertsson, J. (2018). 6-C polarization analysis using point measurements of translational and rotational ground-motion: theory and applications. *Geophysical Journal International*, 213, 77–97. <https://doi.org/10.1093/gji/ggx542>
- Sollberger, D., Igel, H., Schmelzbach, C., Edme, P., van Manen, D.-J., Bernauer, F., et al. (2020). Seismological processing of six degree-of-freedom ground-motion data. *Sensors*, 20(23). <https://doi.org/10.3390/s20236904>
- Sollberger, D., Schmelzbach, C., Renterghem, C. V., Robertsson, J. O. A., & Greenhalgh, S. A. (2015). Geophone coupling corrections for land-seismic point receiver acquisition: 77th annual international conference and exhibition. *EAGE, Extended Abstracts*. <https://doi.org/10.3997/2214-4609.201412593>
- Spudich, P., & Fletcher, J. (2008). Observation and prediction of dynamic ground strains, tilts, and torsions caused by the M_w 6.0 2004 Parkfield, California, earthquake and aftershocks, derived from UPSAR array observations. *Bulletin of the Seismological Society of America*, 98, 1898–1914. <https://doi.org/10.1785/0120070157>
- Spudich, P., Steck, L. K., Hellweg, M., Fletcher, J. B., & Baker, L. M. (1995). Transient stresses at Parkfield, California produced by the M7.4 Landers earthquake of June 28, 1992: Observations from the UPSAR dense seismograph array. *Journal of Geophysical Research*, 100, 675–690. <https://doi.org/10.1029/94JB02477>
- Suryanto, W., Igel, H., Wassermann, J., Cochard, A., Schuberth, B., Vollmer, D., et al. (2006). First comparison of array-derived rotational ground motions with direct ring laser measurements. *Bulletin of the Seismological Society of America*, 96, 2059–2071. <https://doi.org/10.1785/0120060004>
- Takeo, M., & Ito, H. M. (1997). What can be learned from rotational motions excited by earthquakes? *Geophysical Journal International*, 129, 319–329. <https://doi.org/10.1111/j.1365-246X.1997.tb01585.x>
- Tanimoto, T., Hadziioannou, C., Igel, H., Wasserman, J., Schreiber, U., & Gebauer, A. (2015). Estimate of Rayleigh-to-Love wave ratio in the secondary microseism by colocated ring laser and seismograph. *Journal of Geophysical Research*, 120, 2650–2655. <https://doi.org/10.1002/2015GL063637>
- Tiira, T., Janik, T., Skrzynik, T., Komminaho, K., Heinonen, A., Veikkolainen, T., et al. (2020). Full-scale interpretation of Kokkola-Kymi (KOKKY) seismic profile, Fennoscandian Shield. *Pure and Applied Geophysics*, 177, 3775–3795. <https://doi.org/10.1007/s00024-020-02459-3>
- Trifunac, M. D., & Todorovska, M. I. (2001). A note on the useable dynamic range of accelerographs recording translation. *Geophysical Journal International*, 21, 275–286. [https://doi.org/10.1016/S0267-7261\(01\)00014-8](https://doi.org/10.1016/S0267-7261(01)00014-8)
- van Driel, M., Wassermann, J., Nader, M. F., Schuberth, B. S. A., & Igel, H. (2012). Strain rotation coupling and its implications on the measurement of rotational ground motions. *Journal of Seismology*, 16, 657–668. <https://doi.org/10.1007/s10950-012-9296-5>
- Wagner, G. S. (1998). Local wave propagation near the San Jacinto fault zone, southern California: Observations from a three-component seismic array. *Journal of Geophysical Research*, 103(B4), 7231–7246.
- Wassermann, J., Wietek, A., Hadziioannou, C., & Igel, H. (2016). Toward a single-station approach for microzonation: Using vertical rotation rate to estimate Love-wave dispersion curves and direction finding. *Bulletin of the Seismological Society of America*, 106, 1316–1330. <https://doi.org/10.1785/0120150250>
- Wielandt, E. (2012). Seismic sensors and their calibration. In P. Bormann, Ed., *New manual of seismological observatory practice (NMSOP-2)*. Potsdam. GFZ German Research Centre for Geosciences. <https://doi.org/10.2312/GFZ.NMSOP-2>